JOURNAL OF PROPULSION AND POWER
Vol. 13, No. 5, September–October 1997

Flammability Limits and Probability Density Functions in Simulated Solid-Fuel Ramjet Combustors

Tong-Miin Liou,* Wan-Yih Lien,† and Po-Wen Hwang‡
National Tsing Hua University, Hsinchu, Taiwan 30043, Republic of China

A numerical analysis was performed to study turbulent reacting flows in solid-fuel ramjet combustors. The time-dependent axisymmetric compressible conservation equations were solved with a subgrid-scale turbulence model. The combustion process considered was a one-step, irreversible, and infinitely fast chemical reaction. The numerical code used the finite volume technique, which involved alternating in time the second-order, explicit MacCormack's and modified Godunov's schemes. Computed temperature profiles are compared with existing experimental data and the previous calculations, incorporating the k-ε turbulence model and two-layer near-wall treatment. The superiority of the present predictions is demonstrated. Flammability limits in solid-fuel ramjet combustors have been determined using the characteristic exhaust velocity. Moreover, a compact correlation relating the minimum step height to the combustor diameter, air mass flow rate, and equivalence ratio for sustained combustion is provided for practical design reference. Probability density function (PDF) profiles of temperature and mixture fraction are also analyzed to understand the thermal structure of turbulent flames, and to provide information for examining the applicability of the conserved-scalar approach incorporated PDF models to turbulent-reacting flows.

Nomenclature

A_t = throat area
C_p = specific heat at constant pressure, kJ/(kg·K)
c_k = model constant
c_s = Smagorinsky constant
c^* = characteristic exhaust velocity, m/s
D = combustor diameter, m
D_P = near-wall damping function
$\boldsymbol{F}$ = convective flux vector in x direction of Navier–Stokes equations
F/O = fuel air ratio
f = mixture fraction, $(\xi - \xi_a)/(\xi_{\text{fu}} - \xi_a)$
G = spatial filter function
$\boldsymbol{G}$ = convective flux vector in y direction of Navier–Stokes equations
g = flow variable
H = total enthalpy, kJ/kg
H^0_{fu} = heat of reaction, kJ/kg
h = step height, m
k_s = turbulence kinetic energy of the subgrid scales, m^2/s^2
L = combustor length, m
$\dot{m}$ = mass flow rate, g/s
N_a = airflow rate, g mole/s
p = pressure, N/m^2
$\boldsymbol{Q}$ = conservation variables vector of Navier–Stokes equations
q_s = subgrid-scale heat flux, W/m^2
Re_h = Reynolds number, $\langle \tilde{u}_a \rangle \cdot h/\nu$
R_u = universal gas constant
r = radial coordinate
$\dot{r}$ = regression rate, mm/s
$\boldsymbol{S}$ = source term
Sc_s = subgrid-scale Schmidt number
S_{ij} = $\frac{1}{2}(\partial u_i/\partial x_j + \partial u_j/\partial x_i) - \frac{1}{3}\delta_{ij}(\partial u_k/\partial x_k)$, strain rate tensor
T = temperature, K
t = time coordinate, s
u = velocity in x direction, m/s
u_τ = $\sqrt{\tau_w/\bar{\rho}}$, friction velocity, m/s
u^+ = $\tilde{u}/u_\tau$
V = reactor volume, l
v = velocity in r direction, m/s
W = molecular weight, kg
x = axial coordinate
Y = mass fraction
y = radial coordinate
y^+ = yu_τ/ν, dimensionless distance from walls
Γ = diffusivity of species, kg/(m·s)
γ = specific heats ratio
Δ = filter width
δ_{ij} = Kronecker delta function
ε = dissipation rate of turbulence kinetic energy, m^2/s^3
ζ = dummy variable
θ_s = subgrid-scale scalar flux, kg/(m^2·s)
μ = dynamic viscosity, kg/(m·s)
ν = kinematic viscosity, m/s^2
ν_s = subgrid kinematic viscosity, m/s^2
ξ = variable of conserved property
ρ = density, kg/m^3
τ = viscous shear stress, N/m^2
τ_s = subgrid-scale shear stress, N/m^2
τ_w = shear stress at wall, N/m^2
ϕ = equivalence ratio, $(F/O)/(F/O)_{\text{st}}$
ψ = stream function
Ω = flow domain

Subscripts
a = air
c = chamber
e = chamber exit
fu = fuel
i = species
max = maximum
min = minimum
re = reattachment

Received June 28, 1996; revision received April 7, 1997; accepted for publication April 17, 1997.

*Professor, Department of Power Mechanical Engineering. E-mail: tmliou@tmp.nthu.edu.tw.
†Ph.D., Department of Power Mechanical Engineering.
‡Graduate Student, Department of Power Mechanical Engineering.

sr = stirred reactor
st = stoichiometric condition

Superscripts
′ = subgrid component
″ = mass-weighted subgrid component
‴ = temporally fluctuating value of variables
− = spatially filtered quantity
~ = mass-weighted spatially filtered quantity
⟨ ⟩ = time-averaged quantity

Introduction

THE solid-fuel ramjet (SFRJ), a design that comprises the high performance of a conventional liquid-fuel ramjet and the simplicity of a solid propellant rocket motor, offers significant advantages when cost, simplicity, and performance are considered. The present work focuses on the study of turbulent reacting flows in an SFRJ combustor. The SFRJ combustor (Fig. 1) is basically a cylindrical grain with the coaxial incoming air flowing through the fuel port. Sudden expansion of the incoming air generates a separated recirculation zone necessary for flame stabilization. Immediately downstream of the recirculation region, a diffusion flame between the fuel gasification products and the air is established within the developing turbulent boundary layer.

A number of investigations have described the flow and combustion processes in an SFRJ combustor. Researchers at the U.S. Naval Postgraduate School have carried out both numerical[1,2] and experimental[3–6] work. A joint research program has been conducted both numerically[7,8] and experimentally[9] at the Delft University of Technology and the Prins Maurits Laboratory in The Netherlands. Researchers at the Technion in Israel[10–13] and at the German Aerospace Research Establishment in Germany[14,15] have been focusing on experimental work. The previously mentioned experimental work mainly studied the reattachment length, fuel regression rate, and flame stabilization in SFRJ combustors.

A detailed discussion of the aforementioned numerical simulations has been given[16] and will not be repeated here. Basically, these previous computations adopted two-equation type turbulence models, and a standard or modified wall function for the near-wall treatment. However, whether the wall function can be applied to the flowfield in an SFRJ combustor remains an open question because there exists a recirculation zone behind the inlet step and mass addition through the fuel surface. The results calculated by Vos[8] showed that the wall function works satisfactorily for only relatively small fuel blowing velocities ($\tilde{v}_{fu} \leq 0.05$ m/s), and $\tilde{v}_{fu}$ used by Elands[7] was limited within 0.1 m/s; whereas the range of $\tilde{v}_{fu}$ of an actual SFRJ is approximately 0.1–0.5 m/s (Ref. 14). Consequently, there is a need to develop other numerical methods that can simulate the turbulent reacting flowfields in an SFRJ combustor for a higher $\tilde{v}_{fu}$ range. In addition, all the previous numerical simulations employ a steady-state formulation, while the flow and combustion processes in an SFRJ combustor are highly time dependent. Liou et al.[16] attempted to solve the time-dependent, axisymmetric compressible conservation equations directly without subgrid-scale turbulence models, and demonstrated the applicability of their numerical method to the study of turbulent nonreacting and reacting flows in an SFRJ combustor for $0.1 \leq \tilde{v}_{fu} \leq 0.8$ m/s. The present work extends the calculations to include subgrid-scale (SGS) turbulence models and to attain the following goals: 1) to further verify our computational code in terms of a comparison of calculated temperature profiles with those measured by Schulte et al.[15] in an SFRJ combustor; 2) to determine the flammability limits of an SFRJ combustor; and 3) to correlate a compact relation among the minimum step height, air mass flow rate, and equivalence ratio for design reference.

Governing Equations and Numerical Algorithm

In the current simulations, the flow variables are decomposed into a large-scale (or resolved) part that can be solved explicitly, and a SGS part that is modeled with a SGS model. The filtering operation

$$\bar{g}(\boldsymbol{x}) = \int_{\Omega} G_{\Delta}(\boldsymbol{x} - \zeta) g(\zeta)\, \mathrm{d}\zeta \tag{1}$$

where G is a filter function of volume averaging,[17] decomposes

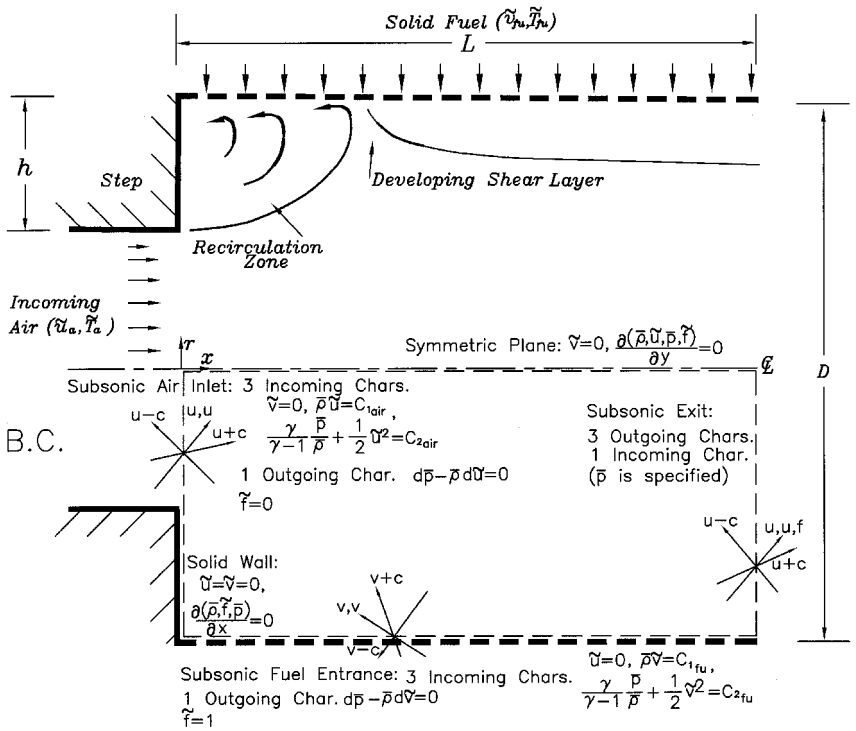

Fig. 1 Schematic illustration of flow pattern and boundary conditions in a solid-fuel combustion chamber.

a variable g into a large-scale component $\bar{g}$ and a SGS component g', which accounts for the scales not resolved by Δ:

$$g = \bar{g} + g' \tag{2}$$

A mass-weighted filter that simplifies the mathematical expressions for compressible flow simulations is defined by

$$\tilde{g} = \overline{\rho g}/\bar{\rho} \tag{3}$$

This implies a second decomposition of g:

$$g = \tilde{g} + g'' \tag{4}$$

The pyrolizing solid fuel is simulated by gaseous ethylene (C_2H_4), radially injected through a porous wall,[15,18] and the chemical reaction is assumed to be infinitely fast and one step; hence, the combustion process is limited by the mixing of fuel and airstreams. Under the assumption of diffusion-flame, no external heat additions, and body forces, the filtered forms of compressible mass, momentum, and mixture fraction equations with the Smagorinsky SGS eddy viscosity model,[19] in two-dimensional axisymmetric coordinates, can be respectively written as

$$\frac{\partial \bar{\rho}}{\partial t} + \frac{\partial}{\partial x}(\bar{\rho}\tilde{u}) + \frac{1}{r}\frac{\partial}{\partial r}(r\bar{\rho}\tilde{v}) = 0 \tag{5}$$

$$\frac{\partial}{\partial t}(\bar{\rho}\tilde{u}) + \frac{\partial}{\partial x}(\bar{\rho}\tilde{u}\tilde{u} - \bar{\tau}_{xx} - \tau_{s_{xx}}) + \frac{1}{r}\frac{\partial}{\partial r}[r(\bar{\rho}\tilde{u}\tilde{v} - \bar{\tau}_{xr} - \tau_{s_{xr}})] = 0 \tag{6}$$

$$\frac{\partial}{\partial t}(\bar{\rho}\tilde{v}) + \frac{\partial}{\partial x}(\bar{\rho}\tilde{v}\tilde{u} - \bar{\tau}_{rx} - \tau_{s_{rx}}) + \frac{1}{r}\frac{\partial}{\partial r}[r(\bar{\rho}\tilde{v}\tilde{v} - \bar{\tau}_{rr} - \tau_{s_{rr}})] + \frac{1}{r}\left[-\bar{p} - \left(\frac{2}{3}\right)\mu\nabla\cdot\boldsymbol{V} + 2\mu\tilde{v}/r\right] = 0 \tag{7}$$

$$\frac{\partial \bar{\rho}\tilde{f}}{\partial t} + \frac{\partial}{\partial x}\left(\bar{\rho}\tilde{u}\tilde{f} - \Gamma\frac{\partial \tilde{f}}{\partial x} - \theta_{s_x}\right) + \frac{1}{r}\frac{\partial}{\partial r}\left[r\left(\bar{\rho}\tilde{v}\tilde{f} - \Gamma\frac{\partial \tilde{f}}{\partial r} - \theta_{s_y}\right)\right] = 0 \tag{8}$$

where viscous stresses τ_{ij} are defined as

$$\tau_{xx} = -p + 2\mu\left[\frac{\partial u}{\partial x} - \frac{1}{3}\left(\frac{\partial u}{\partial x} + \frac{\partial v}{\partial r} + \frac{v}{r}\right)\right]$$

$$\tau_{rr} = -p + 2\mu\left[\frac{\partial v}{\partial r} - \frac{1}{3}\left(\frac{\partial u}{\partial x} + \frac{\partial v}{\partial r} + \frac{v}{r}\right)\right]$$

$$\tau_{xr} = \tau_{rx} = \mu\left(\frac{\partial u}{\partial r} + \frac{\partial v}{\partial x}\right)$$

The terms $\tau_{s_{ij}}$ and θ_{s_j} are the SGS stresses and scalar fluxes, respectively, and can be modeled as

$$\tau_{s_{xx}} = \bar{\rho}(\tilde{u}\tilde{u} - \widetilde{uu}) = 2\bar{\rho}\nu_s\left[\frac{\partial \tilde{u}}{\partial x} - \frac{1}{3}\left(\frac{\partial \tilde{u}}{\partial x} + \frac{\partial \tilde{v}}{\partial r} + \frac{\tilde{v}}{r}\right)\right] - \frac{2}{3}\bar{\rho}k_s$$

$$\tau_{s_{yy}} = \bar{\rho}(\tilde{v}\tilde{v} - \widetilde{vv}) = 2\bar{\rho}\nu_s\left[\frac{\partial \tilde{v}}{\partial y} - \frac{1}{3}\left(\frac{\partial \tilde{u}}{\partial x} + \frac{\partial \tilde{v}}{\partial r} + \frac{\tilde{v}}{r}\right)\right] - \frac{2}{3}\bar{\rho}k_s$$

$$\tau_{s_{xy}} = \tau_{s_{yx}} = \bar{\rho}(\tilde{u}\tilde{v} - \widetilde{uv}) = \bar{\rho}\nu_s\left(\frac{\partial \tilde{u}}{\partial r} + \frac{\partial \tilde{v}}{\partial x}\right)$$

$$\theta_{s_x} = \bar{\rho}(\tilde{f}\tilde{u} - \widetilde{fu}) = \frac{\bar{\rho}\nu_s}{Sc_s}\frac{\partial \tilde{f}}{\partial x}$$

$$\theta_{s_y} = \bar{\rho}(\tilde{f}\tilde{v} - \widetilde{fv}) = \frac{\bar{\rho}\nu_s}{Sc_s}\frac{\partial \tilde{f}}{\partial r}$$

where ν_s and k_s, prescribed by the Smagorinsky model, are

$$\nu_s = (c_s D_p \Delta)^2\left(2\tilde{S}_{ij}\frac{\partial \tilde{u}_i}{\partial x_j}\right)^{1/2} \qquad k_s = \nu_s^2/(c_k\Delta)^2$$

c_s(=0.15) (Ref. 20) and c_k(=0.094) are model constants, Δ is the average size of the computational cell, and D_P is (Ref. 21) expressed as

$$D_P = 1 - \exp[-(y^+)^3/25^3]$$

Equations (5)–(8) can be put into the following general form:

$$\frac{\partial \boldsymbol{Q}}{\partial t} + \frac{\partial \boldsymbol{F}}{\partial x} + \frac{1}{r}\frac{\partial}{\partial r}(r\boldsymbol{G}) + \frac{\boldsymbol{S}}{r} = 0 \tag{9}$$

f is defined as

$$f = (\xi - \xi_a)/(\xi_{\text{fu}} - \xi_a) \tag{10}$$

where the variable ξ represents any conserved property free from sources and sinks. For an adiabatic flow, the total enthalpy can be directly obtained by

$$H = H_a + \tilde{f}(H_{\text{fu}} - H_a) \tag{11}$$

without solving the energy equation. H is defined as

$$H = \tilde{Y}_{\text{fu}}H^0_{\text{fu}} + \sum_i \int_{\tilde{T}_0}^{\tilde{T}} \tilde{Y}_i C_{p_i}\,\mathrm{d}\tilde{T} + \frac{1}{2}(\tilde{u}^2 + \tilde{v}^2) \tag{12}$$

Once $\tilde{f}$, together with $\bar{\rho}$, $\tilde{u}$, and $\tilde{v}$, are solved from the governing equations [Eqs. (5)–(8)], $\tilde{Y}_i$ can be obtained from Eq. (10), and the temperature can be directly calculated from Eqs. (11) and (12). Finally, the equation of state determines the pressure from the temperature, density, and species mass fractions:

$$\bar{p} = \bar{\rho}R_u\tilde{T}\sum_{i=1}^{n}\tilde{Y}_i/W_i \tag{13}$$

The values of heat of reaction, specific heat, and molecular weights of gaseous ethylene are based on the data of Vanka et al.[22] The numerical code uses the finite volume technique that involves alternating in time the second-order, explicit MacCormack's and modified Godunov's schemes. A reduction in phase error can be achieved by temporal switching of these two schemes, since MacCormack's scheme has a lagging phase error and Godunov's scheme has a leading phase error.[23] A detailed description of the numerical algorithm, boundary, and initial conditions is available in Liou et al.[16]

Results and Discussion

Grid Independence and Code Validation

Before comparing the computed results with the experimental data, grid independence is first investigated by checking the mean effective reattachment length (x_{re}) (Ref. 16) and temperature distribution. The time-averaging is performed by $\langle\tilde{g}\rangle = \int_0^T \tilde{g}\,\mathrm{d}t/T$, where $T = 0.015$ s. Four sets of uniform grids,

102 × 12, 202 × 22, 302 × 32, and 402 × 42 ($x \times y$), are examined, and the grid independence is attained for grid sizes of 302 × 32 and 402 × 42. The deviations in x_{re} calculated from these two grid systems are only 0.85 and 0.92%, for the nonreacting and reacting flows, respectively; the deviations of the mean temperature along the radial coordinate at $x/D = 0.6$, 1.7, and 5 are all less than 1%. Consequently, the results presented next are based on the 302 × 32 grid system.

The experimental conditions of Boaz[18] and Schulte et al.[15] (Table 1), are used as an initial input of the present calculations for code validation. A comparison of x_{re}/D vs h/D between the calculations using the present method, Elands's computations,[7] and Boaz's measurements,[18] for both nonreacting and reacting flows, has been reported by Liou et al.[16] The computed results of Liou et al.[16] achieve a practical improvement in predicting x_{re}. A further comparison for the radial mean temperature profiles at three axial locations, $x/D = 0.6$ (in the recirculation zone), $x/D = 1.7$ (near x_{re}), and $x/D = 5$ (downstream of x_{re}), is depicted in Fig. 2. In Fig. 2, the measurements were made by Schulte et al.,[15] and the results of Elands et al.[24] were obtained using the k-ε turbulence model with a two-layer near-wall treatment and turbulent diffusion flame model. It is noticed that the computed temperature profiles of Elands et al.[24] in the recirculation zone is not available, possibly because of the inadequacy of the k-ε turbulence model with wall functions in this region. Again, a significant improvement is gained in predicting the peak mean temperature, especially at $x/D = 1.7$ and 5.

Table 1 Experimental conditions used for specifying initial conditions in the calculations

X_{re} validation[18]	T profiles validation[15]
$h = 0.015$ m	$h = 0.015$ m
$h/D = 0.25$	$h/D = 0.25$
$L = 0.3$ m	$L = 0.3$ m
$\tilde{u}_a = 162$ m/s	$\tilde{u}_a = 78.67$ m/s
$Re_h = 7.2 \times 10^4$	$Re_h = 1.5734 \times 10^4$
$\tilde{v}_{fu} = 0.1$ m/s	$\dot{r} = 0.257$ mm/s
$\tilde{T}_a = 300$ K	$\tilde{T}_a = 473$ K
$\tilde{T}_{fu} = 800$ K	$\tilde{T}_{fu} = 800$ K
$\tilde{Y}_{O_2} = 0.231$	$\tilde{Y}_{O_2} = 0.21$
$\tilde{Y}_{N_2} = 0.769$	$\tilde{Y}_{N_2} = 0.79$
$\tilde{Y}_{fu} = 0.25$	$\tilde{Y}_{fu} = 0.35$
$\bar{p}_c = 4.2 \times 10^5$ N/m^2	$\bar{p}_c = 5.2 \times 10^5$ N/m^2

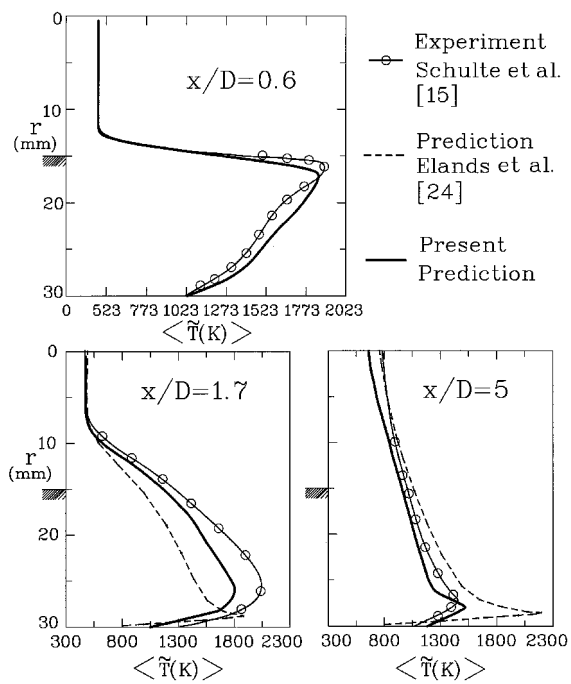

Fig. 2 Comparison of computed time-averaged radial temperature profiles with previous predictions and measured data at three axial locations.

The streamwise evolution of mean temperature distribution in an SFRJ combustor can also be understood from Fig. 2. Immediately downstream of the flameholder step, a rapid increase of the air inlet temperature from 473 K (200°C) to a maximum temperature of 1873 K (1600°C) occurs at $x/D = 0.6$ in the separated shear layer, where the air and fuel mixing is most vigorous. As the flow proceeds further downstream, the peak temperature moves toward the porous wall because of the shear layer's curving down; the more uniform radial temperature distribution across the recirculation zone at $x/D = 1.7$ suggests that the separated recirculating zone plays the flame-holding role. The two previously mentioned profiles reveal that the combustion process takes place mainly in the shear layer between the axial incoming air flow and the recirculation zone. In contrast, the profile downstream of the recirculation zone, $x/D = 5$, indicates that the maximum temperature occurs close to the fuel-injection wall. At $x/D = 5$, the core flow temperatures for the prediction are slightly low in comparison to the experiments of Schulte et al.[15] This is attributable to a prediction of flame front closer to the fuel-injection wall (Fig. 2), which results in a reduction of heat transfer to the core flow and, in turn, a lower core flow temperature prediction.

From the previous discussion, the present calculated results are in reasonably good agreement with the measured mean effective reattachment length and temperature distribution. This fact lends reasonable confidence to the following analyses.

Flammability Limits

The characteristic exhaust velocity c^* has frequently been used in measuring the merit of combustion chamber properties, and can be expressed as follows:

$$c^* = \langle \bar{p}_c \rangle A_t / \dot{m}_e = \frac{(\gamma R \langle \tilde{T}_c \rangle)^{0.5}}{\gamma \{[2/(\gamma+1)]^{(\gamma+1)/(\gamma-1)}\}^{0.5}} \qquad (14)$$

c^* is easily determined from measured $\dot{m}_e$, $\langle \bar{p}_c \rangle$, and A_t, or from hot combustion gas properties (γ, R, and $\langle \tilde{T}_c \rangle$). c^*, calculated from Eq. (14), is generally in good agreement with the actual experimental value and has been used in design calculations.[25] Figure 3 shows the computed c^* as a function of $\dot{m}_a$ for various $\tilde{v}_{fu}$ and fixed value of $h/D = 0.25$. It can be seen that along a line of constant $\tilde{v}_{fu}$, there is a steep descent in c^*, implying a dramatic drop in combustion efficiency as $\dot{m}_a$ exceeds a critical value. From Fig. 3, $c^* = 775$ m/s, which is close to the experimental value $c^* = 800$ m/s of Elands et al.,[26] can be considered as the flammability limit in the present study. The region above $c^* = 775$ m/s is defined here as a

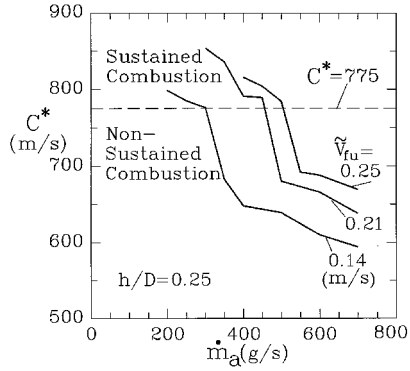

Fig. 3 Time-averaged characteristic exhaust velocity as a function of $\dot{m}_a$ for various $\tilde{v}_{fu}$.

sustained combustion, whereas the region below $c^* = 775$ m/s is a nonsustained combustion.

Figure 4 compares the mean temperature distributions of nonsustained and sustained combustion for $\tilde{v}_{fu} = 0.21$ m/s and $h/D = 0.25$. The high-temperature zone is found only to prevail very near the backward-facing step for the case of nonsustained combustion (in mass flow rate $\dot{m}_a = 500$ g/s in Fig. 3), which is insufficient to support a flame-holding condition and, therefore, produces a low value of c^* in Fig. 3. For the case of sustained combustion ($\dot{m}_a = 450$ g/s in Fig. 3), there exists a much larger high-temperature zone behind the step as compared with the nonsustained combustion case, which provides a good flame-holding condition.

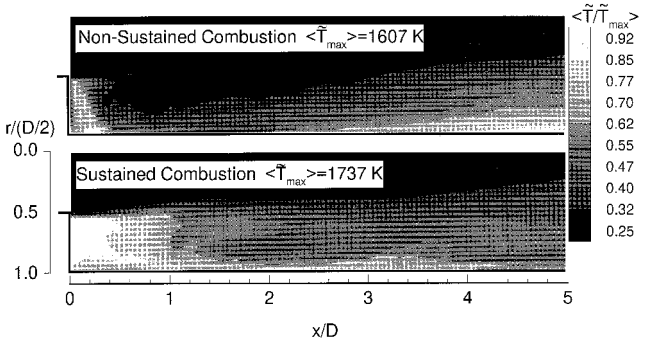

Fig. 4 Time-averaged mean temperature distributions for nonsustained and sustained combustion, with $\tilde{v}_{fu} = 0.21$ m/s and $h/D = 0.25$.

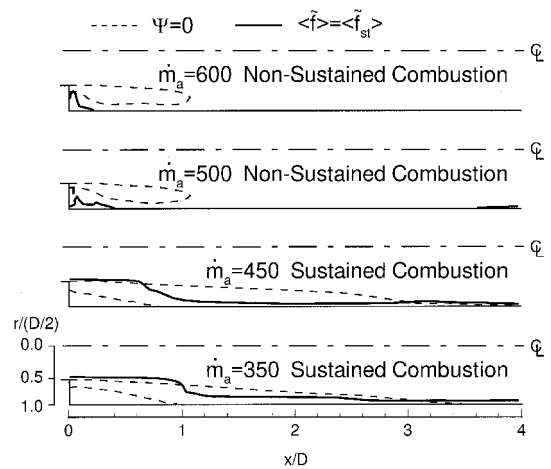

Fig. 5 Time-averaged mean recirculation zone ($c = 0$) and flame sheet ($\langle \tilde{f} \rangle = \langle \tilde{f}_{st} \rangle$) for various $\dot{m}_a$ with $\tilde{v}_{fu} = 0.21$ m/s and $h/D = 0.25$.

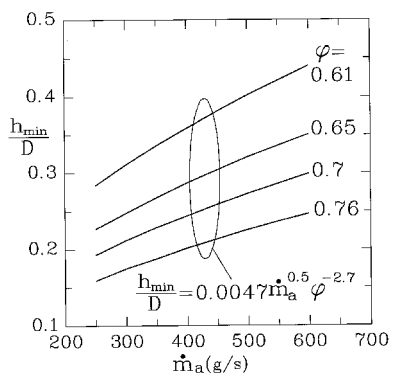

Fig. 6 Correlation of the time-averaged minimum step height to combustor diameter, air mass flow rate, and equivalence ratio for sustaining combustion.

To further understand the main difference between nonsustained and sustained combustion, it is instructive to examine from Fig. 5 how the mean recirculation zone ($\psi = 0$) size and flame sheet ($\langle \tilde{f} \rangle = \langle \tilde{f}_{st} \rangle$) location vary with $\dot{m}_a$ for $\tilde{v}_{fu} = 0.21$ m/s and $h/D = 0.25$. For the nonsustained combustion of $\dot{m}_a \geq 500$ g/s in Fig. 3, the wall-injected fuel flow cannot penetrate into the recirculation zone, and the mean flame sheet thus appears only in a narrow region near the step corner, a poor flame-holding condition. On the contrary, for the sustained combustion of $\dot{m}_a \leq 450$ g/s in Fig. 3, the wall-injected fuel flow can penetrate deeper into the airstream, and the mean flame sheet is therefore located at a larger distance from the fuel surface. In addition, the recirculation zone size for the

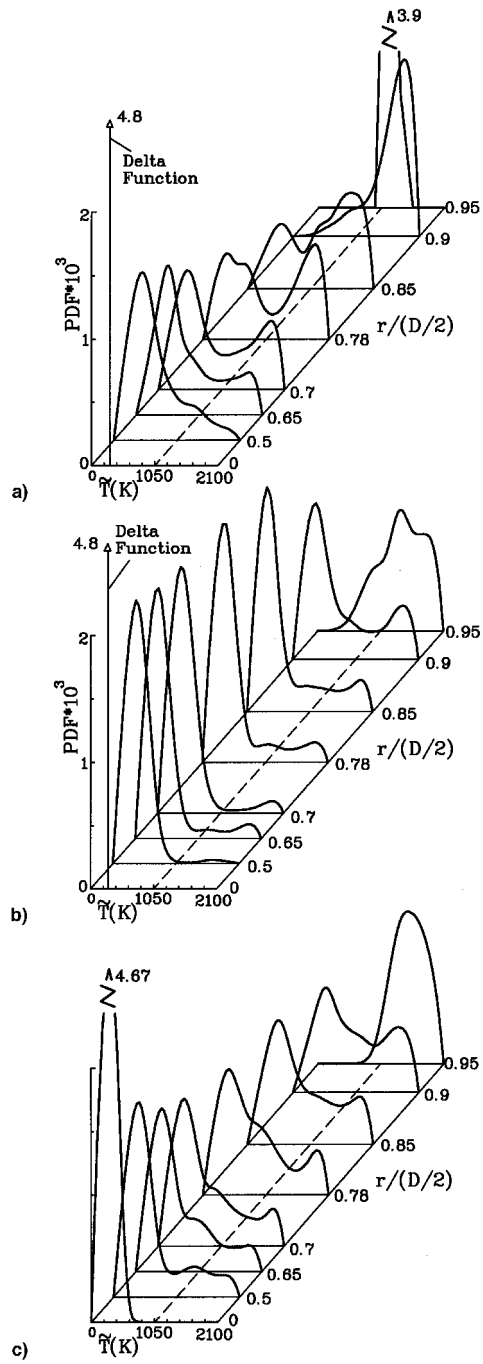

Fig. 7 Radial variations of instantaneous temperature PDF profiles for $\dot{m}_a = 450$ g/s, $\tilde{v}_{fu} = 0.21$ m/s, and $h/D = 0.25$: a) in the recirculation zone ($x/D = 0.5$), b) near the reattachment point ($x/D = 2$), and c) downstream of the reattachment point ($x/D = 3.5$).

sustained combustion is found to be relatively larger, compared with that for the nonsustained combustion. Moreover, for the sustained combustion, Fig. 5 shows that the mean flame sheet is fully involved in the recirculation zone and even located above the recirculation zone in the region near the inlet step, a mechanism generating a larger high-temperature zone behind the inlet step and providing a good flame-holding condition.

Flame stabilization in an SFRJ is often achieved by forming a backward-facing step at the grain inlet. To achieve sustained combustion, a stable high-temperature recirculation zone is required, as described earlier. The backward-facing step height must be large enough to form the required size of a recirculation zone for a given $\dot{m}_a$ and ϕ in the combustion chamber. However, it is desirable from both pressure loss and fuel loading standpoints that a minimum step height for sustained combustion can be used. This kind of information is plotted in Fig. 6, which shows the minimum value of h/D for a given $\dot{m}_a$ and ϕ to achieve sustained combustion. The curves in Fig. 6 can be further correlated into a single equation:

$$h_{\min}/D = 0.0047(\dot{m}_a)^{0.5}\phi^{-2.7} \tag{15}$$

The differences between the computed results shown in Fig. 6 and Eq. (15) are less than 0.05%. The operating range of $250 \leq \dot{m}_a \leq 600$ g/s in Fig. 6 is based on the air Mach number into an SFRJ combustor, generally in the range of 0.2–0.4. Equation (15), therefore, offers a valuable reference in designing the flame-stabilizer geometry of an SFRJ combustor.

It is desirable to have experimental data reported by other researchers to verify the suitability of Eq. (15). Among the literature surveyed in the Introduction, only Elands et al.[26] investigated the relation between the step height and the flammability limit; three step heights (h = 8, 10, and 12 mm) were examined. Elands et al.[26] computational and experimental results of flammability limits showed an agreement only for the h = 10 mm case. In addition, they provide most detailed information for this case. The validation of Eq. (15) is thus performed for this case. Substituting Elands et al.[26] investigating conditions ($\dot{r}$ = 0.22, Φ = 0.73, and $\dot{m}_a$ = 380) into Eq. (15), one obtains $h_{\min}$ = 9.6 mm, which is close to h = 10 mm. The applicability of Eq. (15) is thus reasonably demonstrated.

Analysis of Probability Density Functions

A detailed description of the scalar fields, such as the probability density function (PDF) profiles of temperature and mixture fraction fluctuations, can afford an effective means to understand the thermal structure of turbulent flames. In addition, a crucial element for turbulent closure of the time-averaged flow equations in many predictive models is the PDF of one or more scalar properties. Generation of the moments of both the property and any function is quite straightforward, once their PDFs have been prescribed.

Temperature PDF

Figure 7 shows the radial variations of temperature PDF profiles at three axial locations for $\dot{m}_a$ = 450 g/s, $\tilde{v}_{fu}$ = 0.21 m/s, and h/D = 0.25. For the temperature PDF profiles at x/D = 0.5 in the recirculation zone (Fig. 7a), it is found that the PDFs in the unburned zone [$r/(D/2) < 0.5$] have peaks at inlet air temperature with a long tail to the high-temperature side, and can be regarded essentially as Delta functions. Moving radially to the fuel surface, the probability of low temperature decreases, whereas that of high temperature increases. At

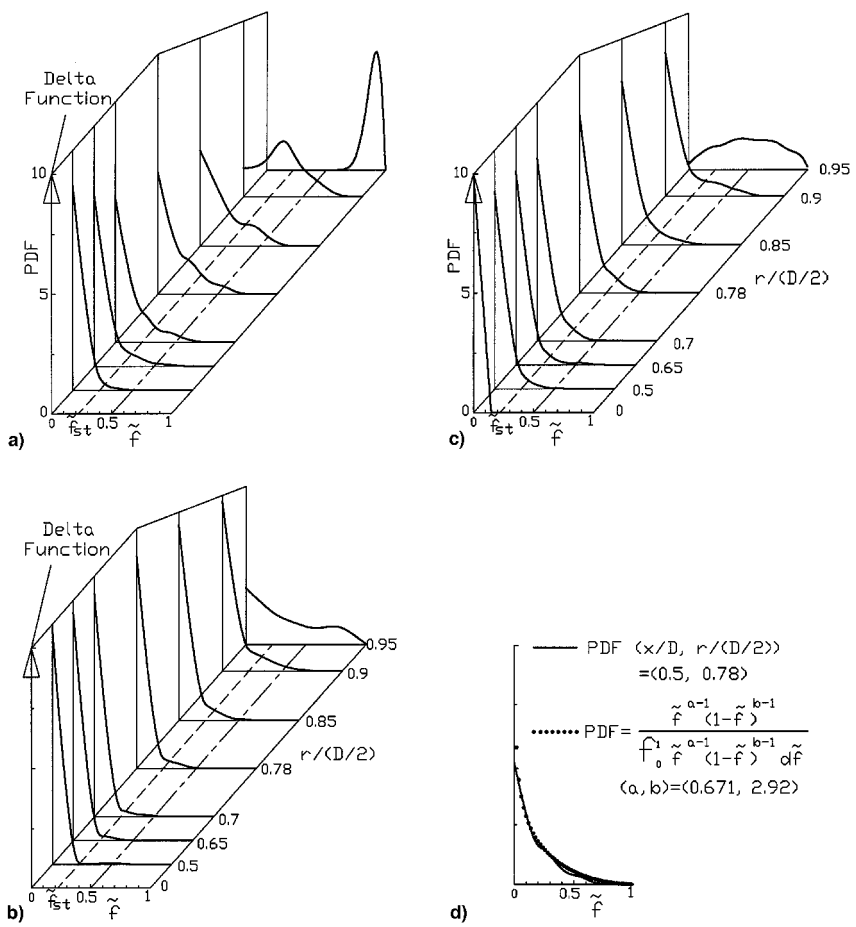

Fig. 8 Radial variations of instantaneous mixture fraction PDF profiles for $\dot{m}_a$ = 450 g/s, $\tilde{v}_{fu}$ = 0.21 m/s, and h/D = 0.25: a) in the recirculation zone (x/D = 0.5), b) near the reattachment point (x/D = 2), c) downstream of the reattachment point (x/D = 3.5), and d) beta function.

$r/(D/2) = 0.78$, the probability of the unburned gas temperature is found to closely approximate that of the burned gas temperature, showing a well-defined bimodal shape[27] and suggesting the presence of the thermal structure of wrinkled laminar flame in the recirculation zone of an SFRJ combustor. However, unlike the turbulent premixed flame in which the bimodal PDFs are dominated by two near-delta functions at essentially two fixed temperatures corresponding to those of the unburned mixture and burned gas, the modal temperatures shown in Fig. 7a evolve significantly with position in the turbulent flame brush. The peak probability of high temperature, in turn, becomes dominant and finally collapses to a narrow spike as the fuel surface is approached. Near the reattachment point ($x/D = 2$), the bimodal shape of temperature PDF profiles is not found and the peak probability of high temperature only appears near the fuel surface (Fig. 7b). In the downstream region of the recirculation zone ($x/D = 3.5$) (Fig. 7c), the well-defined bimodal shape of temperature PDF profiles is not apparent; however, the peak probability of high temperature is found to be more apparent than that at $x/D = 2$.

An examination of the mean flame sheet location may be helpful to gain physical insight into the feature of the temperature PDF distribution discussed earlier. As shown in Fig. 5, for $\dot{m}_a = 450$ g/s, the mean flame sheet penetrates into the recirculation zone around $x/D = 0.5-0.7$, and the fluids recirculation results in a considerable high probability of the burned gas in the region of $0.5 \leq r/(D/2) \leq 1$ (Fig. 7a). At $x/D = 2$, the combustion process prevails close to the fuel surface, since the core flow curves downward near the reattachment point, which illustrates why the probability of high temperature is limited to near the fuel surface (Fig. 7b). At $x/D = 3.5$ the mean flame sheet redevelops and is located at a slightly larger distance from the fuel surface; therefore, the high-temperature burned gas moves slightly upward toward the core region (Fig. 7c).

Mixture Fraction PDF

A solution for the mean and other moments of thermochemical properties, by the conserved scalar approach in a turbulent reacting flow, requires knowledge of that scalar's PDF. In general, the form of the PDF will depend on the flow conditions and will be coupled with the chemical heat release. This dependence might severely limit the application of the conserved-scalar approach to turbulent reacting flows. Figure 8 shows the radial variations of mixture fraction PDF profiles for the same axial locations discussed earlier. A preliminary observation from Fig. 8 shows that the functional form of the PDF varies from point-to-point throughout the flowfield. For example, in the recirculation zone (Fig. 8a), the mixture fraction PDF is a delta function at the centerline of the combustor. Moving toward the fuel surface, the mixture fraction PDF profiles reveal the form of beta functions. Near the fuel surface [$r/(D/2) = 0.95$], a Gaussian-like distribution prevails and the mean fuel fraction is overstoichiometric; and this is responsible for the falling temperature depicted in Fig. 2 as the wall is approached. Near the reattachment point (Fig. 8b), the form of beta functions prevails, except for the centerline region. In the downstream region of the reattachment point (Fig. 8c), beta functions still prevail and a pseudo-Gaussian distribution is found at $r/(D/2) = 0.95$. The functional forms of the mixture fraction PDF are proposed from the present results as beta functions, which will be appropriate for the majority of flowfield in an SFRJ combustor, except for the region near the centerline and fuel surface.

Conclusions

Turbulent reacting flows in an axisymmetric, coaxial sudden-expansion combustion chamber, with gaseous C_2H_4 radially injected through the porous wall, have been simulated numerically for a practical range of fuel blowing velocity encountered in solid-fuel ramjet combustors. A comparison of the present computations with the measured results and previous calculations, incorporating turbulence models and wall functions or two-layer near-wall treatment, demonstrates that the present method achieves a significant improvement in predicting the mean effective reattachment lengths and temperature distribution. The flammability limit has been determined as the minimum value of the characteristic exhaust velocities attaining sustained combustion, and is equal to 775 m/s. The relationship among the minimum ratio of the step height to combustor diameter, air mass flow rate, and equivalence ratio, has been correlated as $h_{\min}/D = 0.0047(\dot{m}_a)^{0.5}\phi^{-2.7}$, for sustained combustion over the practical operating range of air mass flow rate, $250 \leq \dot{m}_a \leq 600$ g/s, in solid-fuel ramjet combustors, which provides a useful reference for the practical design of a solid-fuel ramjet combustor. Furthermore, PDF profiles of temperature and mixture fraction in a SFRJ combustor has been analyzed for the first time. Temperature PDF profiles with bimodal shapes, a phenomenon corresponding to the wrinkled laminar flame model, are observed in the recirculation zone of a SFRJ combustor. For applying the conserved-scalar approach with PDF models to turbulent reacting flows in a SFRJ combustor, the form of beta functions for the mixture fraction PDF is proposed from the present results for the majority of the flowfield.

Acknowledgment

This research was supported by the National Science Council of the Republic of China, Contract NSC 82-0424-E-007-034.

References

[1]Netzer, D. W., "Modeling Solid-Fuel Ramjet Combustion," *Journal of Spacecraft and Rockets*, Vol. 14, No. 12, 1977, pp. 762–766.

[2]Milshtein, T., and Netzer, D. W., "Three-Dimensional, Primitive-Variable Model for Solid-Fuel Ramjet Combustion," *Journal of Spacecraft and Rockets*, Vol. 23, No. 1, 1986, pp. 113–117.

[3]Karadimitris, A., Scott, C., II, and Netzer, D. W., "Regression and Combustion Characteristic of Boron Containing Fuels for Solid-Fuel Ramjets," *Journal of Propulsion and Power*, Vol. 7, No. 3, 1991, pp. 341–347.

[4]Wooldridge, R. C., and Netzer, D. W., "Ignition and Flammability Characteristics of Solid-Fuel Ramjets," *Journal of Propulsion and Power*, Vol. 7, No. 5, 1991, pp. 846–848.

[5]Campbell, W. H., Jr., Ko, B. N., Lowe, S. R., and Netzer, D. W., "Solid-Fuel Ramjet Fuel Regression Rate/Thrust Modulation," *Journal of Propulsion and Power*, Vol. 8, No. 3, 1992, pp. 624–629.

[6]Lee, T. H., and Netzer, D. W., "Temperature Effects on Solid-Fuel Ramjet Fuel Properties and Combustion," *Journal of Propulsion and Power*, Vol. 8, No. 3, 1992, pp. 721–723.

[7]Elands, P. J. M., "The Prediction of the Flow and Combustion in a Solid-Fuel Combustion Chamber by Means of Two Combustion Models Based on the Diffusion Flame Concept," AIAA Paper 87-1702, June 1987.

[8]Vos, J. B., "Calculating Turbulent Reacting Flows Using Finite Chemical Kinetics," *AIAA Journal*, Vol. 25, No. 10, 1987, pp. 1365–1372.

[9]Korting, P., Van der Geld, C., Wijchers, T., and Schoyer, H., "Combustion of PMMA in a Solid-Fuel Ramjet," *Journal of Propulsion and Power*, Vol. 6, No. 3, 1990, pp. 263–270.

[10]Zvuloni, R., Gany, A., and Levy, Y., "Geometric Effects on the Combustion in Solid-Fuel Ramjets," *Journal of Propulsion and Power*, Vol. 5, No. 1, 1989, pp. 32–37.

[11]Zvuloni, R., Levy, Y., and Gany, A., "Investigation of a Small Solid-Fuel Ramjet Combustor," *Journal of Propulsion and Power*, Vol. 5, No. 3, 1989, pp. 269–275.

[12]Netzer, A., and Gany, A., "Burning and Flameholding Characteristics of a Miniature Solid-Fuel Ramjet Combustor," *Journal of Propulsion and Power*, Vol. 7, No. 3, pp. 357–363.

[13]Ben-Arosh, R., and Gany, A., "Similarity and Scale Effects in Solid-Fuel Ramjet Combustors," *Journal of Propulsion and Power*, Vol. 8, No. 3, 1992, pp. 615–623.

[14]Schulte, G., "Fuel Regression and Flame Stabilization Studies of Solid-Fuel Ramjets," *Journal of Propulsion and Power*, Vol. 2, No. 4, 1986, pp. 301–304.

[15]Schulte, G., Pein, R., and Hogl, A., "Temperature and Concentration Measurements in a Solid-Fuel Ramjet Combustion Chamber," *Journal of Propulsion and Power*, Vol. 3, No. 2, 1987, pp. 114–120.

[16]Liou, T. M., Lien, W. Y., and Hwang, P. W., "Large Eddy Simulation of Turbulent Reacting Flows in a Channel with Gaseous Ethylene Injecting Through the Porous Wall," *Combustion and Flame*, Vol. 99, 1994, pp. 591–600.

[17]Yoshizawa, A., "Large-Eddy Simulation of Turbulent Flows," *Encyclopedia of Fluid Mechanics*, Vol. 6, edited by N. P. Cheremisionoff, Gulf Publish Corp., 1986, pp. 1277–1297.

[18]Boaz, L. D., "Internal Ballistics of Solid Fuel Ramjets," M.S. Thesis, U.S. Naval Postgraduate School, Monteres, CA, March 1973.

[19]Smagorinsky, J., "General Circulation Experiments with the Primitive Equations," *Monthly Weather Review*, Vol. 91, No. 3, 1963, pp. 99–164.

[20]Sakamoto, S., Murakami, S., and Mochida, A., "Numerical Study on Flow Past 2D Square Cylinder by Large Eddy Simulation: Comparison Between 2D and 3D Computations," *Journal of Wind Engineering and Industrial Aerodynamics*, Vol. 50, Nos. 1–3, 1993, pp. 61–68.

[21]Piomelli, U., "High Reynolds Number Calculations Using the Dynamic Subgrid-Scale Stress Model," *Physics of Fluids A*, Vol. 5, No. 6, 1993, pp. 1484–1490.

[22]Vanka, S. P., Craig, R. R., and Stull, F. D., "Mixing, Chemical Reaction, and Flowfield Development in Ducted Rockets," *Journal of Propulsion and Power*, Vol. 2, No. 4, 1986, pp. 331–338.

[23]Tsai, Y. P., and Christiansen, W. H., "Two-Dimensional Numerical Simulation of Shear-Layer Optics," *AIAA Journal*, Vol. 28, No. 12, 1990, pp. 2092–2097.

[24]Elands, P. J. M., Korting, P. A. O. G., Wijchers, T., and Dijkstra, F., "Comparison of Combustion Experiments and Theory in Polyethylene Solid-Fuel Ramjets," *Journal of Propulsion and Power*, Vol. 6, No. 6, 1990, pp. 732–739.

[25]Sutton, G. P., "Rocket Propulsion Elements," Wiley, New York, 1986, pp. 55, 56.

[26]Elands, P. J. M., Dijkstra, F., and Zandbergen, B. T. C., "Experimental and Computational Flammability Limits in a Solid-Fuel Ramjet," AIAA Paper 90-1964, July 1990.

[27]Roberts, P. T., and Moss, J. B., "A Wrinkled Flame Interpretation of the Open Turbulent Diffusion Flame," *18th Symposium (International) on Combustion*, edited by the Combustion Inst., Edwards Brothers Inc., MI, 1980, pp. 941–950.